ACS OMEGA

http://pubs.acs.org/journal/acsodf

Article

A Thorough Investigation of Electronic, Optical, Mechanical, and Thermodynamic Properties of Stable Glasslike Sodium Germanate under Compressive Hydrostatic Pressure: Ab Initio Study

Zosiamliana Renthlei, Mattipally Prasad, Juluru Sivakumar, Lalhriat Zuala, Lalrinthara Pachuau, Yengkhom Rangeela Devi, Ningthoujam Surajkumar Singh, Gulmurza Abdurakhmanov, Amel Laref, and Dibya Prakash Rai*

Cite This: *ACS Omega* 2023, 8, 16869−16882

Read Online

ACCESS | Metrics & More | Article Recommendations | Supporting Information

ABSTRACT: In this paper, we have tried to elucidate the variation of structural, electronic, and thermodynamic properties of glasslike Na_2GeO_3 under compressive isotropic pressure within a framework of density functional theory (DFT). The result shows stable structural (orthorhombic → tetragonal) and electronic (indirect → direct) phase transitions at $P \sim 20$ GPa. The electronic band gap transition plays a key role in the enhancement of optical properties. The results of the thermodynamic properties have shown that Na_2GeO_3 follows Debye's low-temperature specific heat law and the classical thermodynamic of the Dulong−Petit law at high temperature. The pressure sensitivity of the electronic properties led us to compute the piezoelectric tensor (both in relaxed and clamped ions). We have observed significant electric responses in the form of a piezoelectric coefficient under applied pressure. This property suggested that Na_2GeO_3 could be a potential material for energy harvest in future energy-efficient devices. As expected, Na_2GeO_3 becomes harder and harder under compressive pressure up to the phase transition pressure (~20 GPa) which can be read from Pugh's ratio (k_H) > 1.75, however, at pressures above 20 GPa k_H < 1.75, which may be due to the formation of fractures at high pressure.

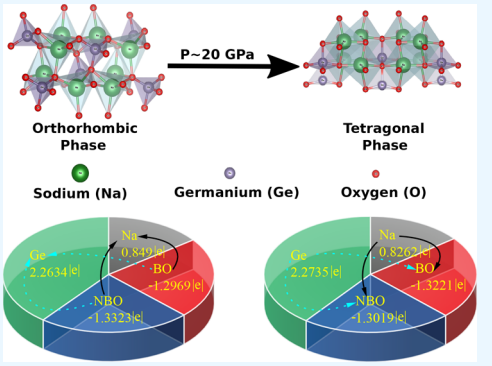

INTRODUCTION

Wide band gap semiconductor materials have received extensive research attention due to their high-temperature structural stability and tunability in electronic and mechanical characteristics.[1−3] Among the wide band gap semiconductors, glasslike materials possessing a band gap ($E_g \geq 2.5$ eV) have become a fascinating material both experimentally and theoretically due to their unique properties such as high mechanical and thermodynamical stabilities, low thermal conductivity, abundant availability in nature, and so on.[4−7] Flexibility in fabrication and reliability of the glass materials have made them promising candidates for technological and industrial uses, particularly in the field of battery and storage systems, fireproof fabrics, fiber optics, electronic device preparation, bioactive glass, substrates for solar cells, etc.[8−12] It is well-known that the majority of the glasses are silica (SiO_2) based material.[13−15] Despite the fact that silicate glasses are the most commonly utilized among different glass types, they have some major drawbacks including their brittleness and impact resistance, property losses at higher temperatures, etc. Therefore, in order to avoid such problems and to use them for a wide range of temperatures, a replacement of silicate glass is necessary. So, alkali germanate glass (Na_2GeO_3) having a high melting point could be a promising replacement for silicate glass.[16−19]

To our knowledge, the structure of Na_2GeO_3 was first determined by Ginetti in 1957 and was later refined by Vollenkle et al.[20,21] Later, more rigorous and detailed work on the structural determination of sodium metagermanate was led by Cruickshank[22] who reported that Na_2GeO_3 has a high structural similarity with Na_2SiO_3.[23] From the work of Cruickshank we have come to know that Na_2GeO_3 exists as an orthorhombic structure with space group $Cmc2_1$ and unit cell lattice parameters of a = 10.845 Å, b = 6.224 Å, and c = 4.918 Å. Recently, Yan et al.[24] prepared a powder form of Na_2GeO_3 by heating a stoichiometric mixture of Na_2CO_3 + GeO_2 → Na_2GeO_3 + CO_2 at 900 °C for 12 h. Analogous to the alkali silicates,[25] the structure of alkali germanate is determined by the presence of a three-dimensional network of

Received: January 25, 2023
Accepted: April 10, 2023
Published: May 4, 2023

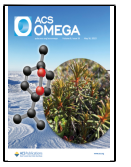

[GeO_4] tetrahedral chain and that of the existence of bridging oxygen (BO) and nonbridging oxygen (NBO) bonds, where alkali atoms are linked. The addition of alkali cation (Na^+) has disrupted the Ge−O−Ge bridging bonds, and as a result, NBO comes into existence. The interesting part of the formation of BO and NBO is that it fully describes most of the structural arrangement of the atoms and defines the atomic level interactions within the compounds.[26] Experimentally, the structure of alkali germanate glass was thoroughly explored and the increase in refractive index and volume density with the increase in alkali oxide was reported. The unique property that germanate glasses exhibit an extrema in physical properties with changes in composition marks them as anomalous compared to their silicate analogues, hence the term germanate anomaly.[27−29] The origin of this anomalous behavior was thought to be due to the conversion of germanium ions from 4-fold to 6-fold symmetry with the increase in alkali concentration. However, the concrete physical interpretation behind such an anomaly is still unexplained. So, in this regard, an advanced computation technique in integration with the standard atomic-scale theory and computer simulations has become a major probe for understanding such behavior.

As far as we are aware, through the surveyed literature, no theoretical works on the electronics, optical, and piezoelectric properties under applied pressures have been performed. Also, the experimental data are only limited to structural and optical properties. In this current work, we have generated the unit cell crystal structure by taking the lattice parameters from the experimental work of Cruickshank.[22] The crystal structure was then optimized for further calculation of the unexplored properties like phase transition, electronic, optical, piezoelectric, and thermodynamic properties under different compressive isotropic pressures up to 25 GPa with a difference of 5 GPa.

COMPUTATIONAL DETAILS

All the computational calculations were performed within the framework of density functional theory (DFT), as implemented in the Vienna ab initio simulation package (VASP).[30] Exchange-correlation was treated within the General Gradient Approximation (GGA) as proposed by Perdew, Burke, and Ernzerhof (PBE).[31] The electron−ion interactions were handled by a Projector Augmented Wave (PAW).[32] The PBE_PAW pseudopotential of Na_pv 19 September 2006 with 7 valence electrons, O 08 April 2002 with 6 valence electrons, and Ge_d 03 July 2007 with 14 valence electrons are sampled for our calculations. The unit cell having 12 atoms with 4 sodium, 2 germanium, and 6 oxygen atoms forms the orthorhombic structure with space group ($Cmc2_1$).[22] For geometry optimization, full-cell optimizations were conducted by relaxing atomic positions, unit cell shape, and unit cell volumes. To ensure the convergence of cell energies and structural parameters, the energy convergence criteria of 10^{-5} eV was set such that the force on each atom was smaller than 0.02 eV/Å. An energy cutoff of 520 eV was adopted for plane-wave expansion of the electronic wave function, and the first Brillouin zone integration was performed using 8 × 8 × 8 k-mesh within the Monkhorst−Pack scheme using a linear-tetrahedron method with Bloechl correction.[33] The above-mentioned geometry convergence criteria were followed for all structures under an isotropic compressive pressure of 0−25 GPa with a difference of 5 GPa. Calculation of phonon dispersion curves along any path through the Brillouin zone are performed based on the so-called direct method requiring an underlying method to calculated forces on atoms. In this work, medeA-Phonon is employed which provides fully automated procedures.[34] During phonon calculations, only the unit cell is considered, and all the single-point calculations for phonon calculations are performed at a standard precision of 500 (equivalent to PREC = Accurate which increases the memory requirements somewhat, but it should be used if very accurate forces (phonons and second derivatives) are required) with a plane wave cutoff of 500 eV, and an electronic iterations convergence of 10^{-5} eV is sampled with 8 × 8 × 8 k-mesh. Moreover, for properties calculation, a dense k-mesh of 12 × 12 × 12 was sampled within the first Brillouin zone.

RESULTS AND DISCUSSION

Structural Properties. Sodium germanate (Na_2GeO_3) has a crystal structure similar to those of sodium silicate (Na_2SiO_3) and lithium germanate (Li_2GeO_3).[35,36] The unit cell exists as an orthorhombic crystal structure with the $Cmc2_1$ space group (Figure 1). The optimized lattice parameters and volumes

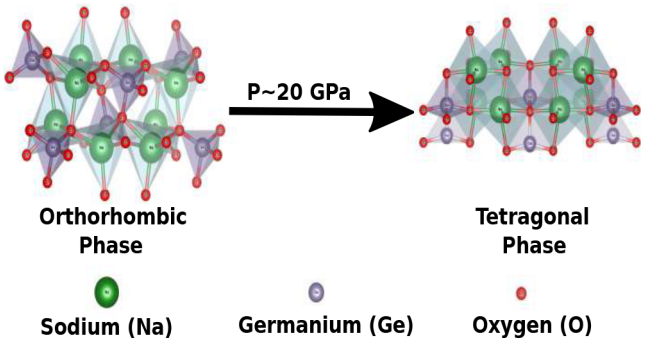

Figure 1. Structural phase transition from orthorhombic to tetragonal under $P \sim 20$ GPa isotropic compressive pressure.

under isotropic pressures with a difference of 5 GPa are given in Table 1. At 0 GPa, our optimized result agrees well with the

Table 1. Optimized Lattice Parameters (Å) and Optimized Volume (Å^3) under Varying Uniform Compressive Isotropic Pressures with a Difference of 5 GPa

Pressure (GPa)	a (Å)	b (Å)	c (Å)	V (Å^3)
0	10.966	6.314	4.995	345.799
	10.845[a]	6.224[a]	4.918[a]	331.962[a]
	10.88[b]	6.21[b]	4.92[b]	332.419[b]
	10.852[c]	6.233[c]	4.960[c]	335.497[c]
5	10.766	6.171	4.808	319.419
10	10.649	6.063	4.660	300.856
15	10.604	5.942	4.543	286.244
20	11.953	4.522	4.520	244.331
20.17	11.943	4.519	4.519	243.943
25	11.948	4.396	4.441	233.223

[a]Reference 22. [b]Reference 37. [c]Reference :43.

experimental data of Cruickshank where the crystal was regrown and 1083 reflexions photographically were collected using a Syntex diffractometer.[22] It also matches with the result of West et al.,[37] where unit cell dimensions were recorded with a Philips Hagg Guinier camera using CuKα radiation, and KCl was added as internal standard. Since the theoretical works are limited for this compound, we have these available

https://doi.org/10.1021/acsomega.3c00499
ACS Omega 2023, 8, 16869−16882

experimental data for structural parameter comparison. However, many DFT works has already been performed on Na_2SiO_3 and Li_2GeO_3 that have crystal structures comparable to that of Na_2GeO_3.[38−42] Usually, the lattice parameters obtained for both Na_2SiO_3 and Li_2GeO_3 are smaller than those of Na_2GeO_3 due to the presence of heavier elements. The calculated volume is 4.17% and 4.03% higher than the experimental volumes. The difference in volume is due to the well-known effect of GGA-PBE that overestimates the volumes.

The current work gives a thorough study of the structural deformation of Na_2GeO_3 under isotropic compressive pressures, and variation of lattice parameters with respect to the applied pressure is shown in Figure 2. Interestingly, from

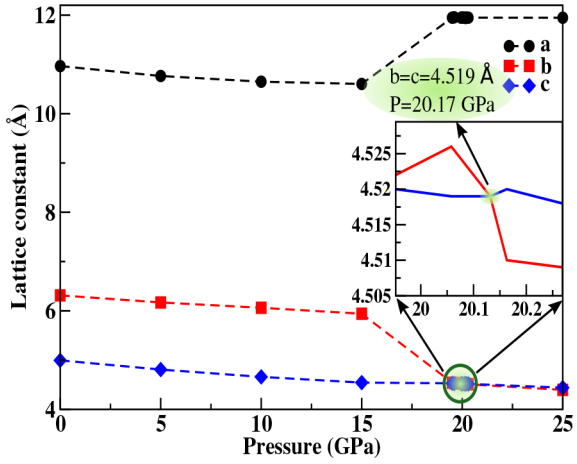

Figure 2. Variation of lattice constants (a,b,c) with pressure. The structural phase transition from orthorhombic phase to the tetragonal phase is obtained at P = 20.17 GPa with $b = c$ = 4.519 Å (see inset).

this study it can be suggested that from a stable orthorhombic phase the next stable phase for this compound could be tetragonal which can be achieved by applying an external pressure. The increase in applied pressure leads to a small variation in the lattice constants up to 15 GPa. At a pressure above 15 GPa we have observed a rapid increase in the lattice constant a while b decreases gradually and there is not much variation in c. The crossover of lattice b and c takes place at 20.17 GPa giving rise to a tetragonal structure ($b = c$ = 4.519 Å). Referring to Table 1, one can find that between 15 and ∼20 GPa the volume of the studied system decreases abruptly, suggesting that it undergoes first-order structural transition. To enrich the structural study, we have calculated the bond length (BL) and bond angle (BA) and observed that at P = 0 GPa the calculated BL and BA are in good agreement with the experimental and theoretical results. Changes in BL and BA with pressure are shown in Table 2. From these results we can understand that the BL are very consistent at all pressures; however, on analyzing the BA for P = 15 and 20 GPa, we observe that Ge−O−Ge BA decreases very rapidly from 114° at 15 GPa to 105.1° at 20 GPa. This confirms that when pressure escalates to around 20 GPa the studied compound has started to undergo a structural phase transition (see Figure 1). For better information on the structural parameters, atomic positions in terms of fractional coordinates at different applied pressures are provided as supplementary data in Table S1.

Electronic Properties. Atomic level interactions in any material are comprehensive by making use of electronic

Table 2. Calculated Bond Length (BL) (Å) Bond angle (BA) (deg) under Different Applied Pressures with a Difference of 5 GPa

P (GPa)	0	5	10	15	20	25
Ge−BO	1.83 (1.80[a]) (1.86[b])	1.81	1.80	1.79	1.86	1.88
Ge−NBO	1.74 (1.71[a]) (1.75[b])	1.73	1.72	1.71	1.73	1.73
Na−BO	2.41 (2.41[a])	2.33	2.28	2.24	2.16	2.16
Na−NBO	2.32 (2.35[a])	2.25	2.20	2.16	2.17	2.15
Ge−O−Ge (deg)	123.6 (124.6[a])	120.1	117.1	114	105.1	103.1

[a]Reference 22. [b]Reference 44.

properties calculations. The calculated band structure and orbital-projected density of states (DOS) of Na_2GeO_3 under different compressive pressures are presented in Figure 3. The zero energy line between the valence and conduction bands is regarded as the Fermi energy level (E_f). The energy dispersions which are shown along the high symmetry points in Figure 3 (e) and (f) are highly different mainly at the valence band region as compared to (a), (b), (c), and (d). Similar to Na_2SiO_3 and Li_2GeO_3,[35,42] the band structures at all different pressures show anticrossing, crossing, and noncrossing behaviors; these consequently create complicated electronic structures. Also, the number of band edges comes into existence in the high-symmetry point that could influence unique van Hove singularities along Γ, R, T symmetry for the studied system at P = 20 and 25 GPa, suggesting a stronger optical absorption.[42,45] From our calculations, between 0 and 15 GPa, the top and bottom of valence and conduction bands are along Z to Γ symmetry points in the first Brillouin zone with indirect band gaps of ∼2.97 3.22, 3.42, and 3.59 eV, respectively. However, at 20 and 25 GPa (after occurrence of structural phase transition), the electronic transition is direct along Γ symmetry points with band gaps of ∼2.87 and 2.80 eV, respectively. Our result at 0 GPa is in good agreement with the recently reported band gap E_g = 3.1 eV.[44] Moreover, it shows a smaller energy gap as compared to Li_2GeO_3 and Na_2SiO_3, where the reported values were usually in the range of 2.97 to 5 eV.[46−48] The investigations of electronic properties for Na_2GeO_3 are very limited; as a result, the present work might provide helpful information for the future. The wide band gap and complex band structure of Na_2GeO_3 have suggested that it has excellent electrochemical stability and also negligible electronic conductivity.[49] Thus, by making use of band gap engineering, if the wide band gap could be reduced so as to enhance its electrical conductivity without losing its electrochemical stability, this compound could be a promising material for semiconductor devices.

The density of states (DOS), which allows us to fully understand the valence and conduction region contribution in the electronic properties study for Na_2GeO_3 at different pressures, are presented in Figure 3. Herein, the DOS are more

https://doi.org/10.1021/acsomega.3c00499
ACS Omega 2023, 8, 16869−16882

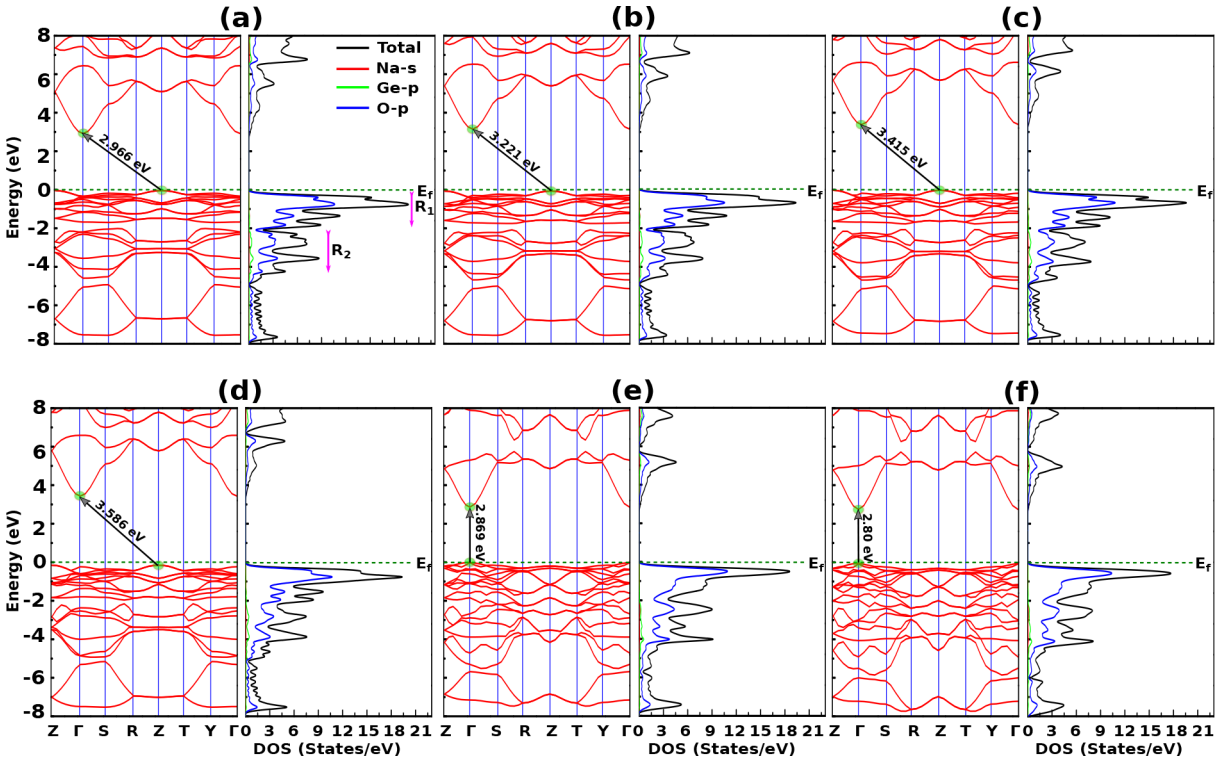

Figure 3. Calculated band structure and density of states (DOS) of Na_2GeO_3: (a) 0 GPa, (b) 5 GPa, (c) 10 GPa, (d) 15 GPa, (e) 20 GPa, and (f) 25 GPa. Here R_1 and R_2 in (a) indicate the first and second regions due to majority contributions from NBO and BO, respectively.

dominated by the valence states ($E < 0$); therefore, the energy spectra of the hole and electron about the Fermi level are highly asymmetric. Generally, the orbital DOS contribution of any compound is highly affected by the change in bond lengths of the neighboring atoms.[50] However, in this study when pressure increases from 0 to 25 GPa the bond lengths are very consistent (see Table 2) so changes in the DOS contributors are not prominent even at different pressures. From the investigation of DOS, it is possible to interpret that the energy states around the top of valence bands are mostly contributed by the O-p state while the energy states near the bottom of conduction bands are contributed mainly by the complex hybridized state of O-p, Ge-p, and Na-s states. In Figure 3 (a), we have presented two main regions in the valence side, denoted as R_1 and R_2; these represent the oxygen contribution on the VB region in terms of NBO and BO, respectively, and are more or less similar to the DOS contribution of BO and NBO in Na_2SiO_3 which was formerly reported by Ching et al.[51] The R_1 within the energy range of 0 to −2 eV are mostly contributed by the NBO, while the R_2 within the energy range of −2 to −5 eV are contributed mainly by the BO. This is due to the effect of relative atomic concentration of BO and NBO where the DOS intensity (States/eV) of BO is about half of NBO, and from a simple altercation of on-site Coulomb repulsion, lower energy (or higher binding energy) of BO valence orbitals should have less electronic valence charge as compared to NBO (see Bader valence charges presented in Table 3 where Bader valence charges of BO are all smaller than that of NBO except at 20 GPa).

Furthermore, we have also presented the calculated Bader charge analysis to examine the charge transfer upon formation of bonds under different compressive pressures. In Table 3, we have presented the Bader valence charge, Bader volume, and Bader charge density at different applied pressures. Clearly, the valence charge density for each atom increases with pressure due to the reduction in the volume with pressure, while that of

Table 3. Calculated Bader Valence Charge (|e|), Bader Volume (in Å^3) and Bader Charge Density (in |e|/Å^3) for Each Atoms under Different Applied Pressures

Pressure (in GPa)	Atom	Valence charge (|e|)	Volume (Å^3)	Bader charge density |e| (Å^3)
	Na	6.142	9.400	0.653
	BO	7.298	16.577	0.440
0	NBO	7.333	20.886	0.351
	Ge	11.752	9.301	1.263
	Na	6.151	8.671	0.709
	BO	7.297	15.424	0.473
5	NBO	7.332	19.096	0.384
	Ge	11.737	8.896	1.319
	Na	6.158	8.166	0.754
	BO	7.309	14.642	0.499
10	NBO	7.330	17.852	0.411
	Ge	11.717	8.536	1.373
	Na	6.164	7.805	0.790
	BO	7.304	13.913	0.525
15	NBO	7.328	16.870	0.434
	Ge	11.714	8.299	1.412
	Na	6.174	7.090	0.871
	BO	7.322	11.389	0.643
20	NBO	7.302	13.866	0.527
	Ge	11.727	7.780	1.507
	Na	6.179	6.814	0.907
	BO	7.282	10.868	0.670
25	NBO	7.296	13.101	0.557
	Ge	11.769	7.609	1.547

https://doi.org/10.1021/acsomega.3c00499
ACS Omega 2023, 8, 16869−16882

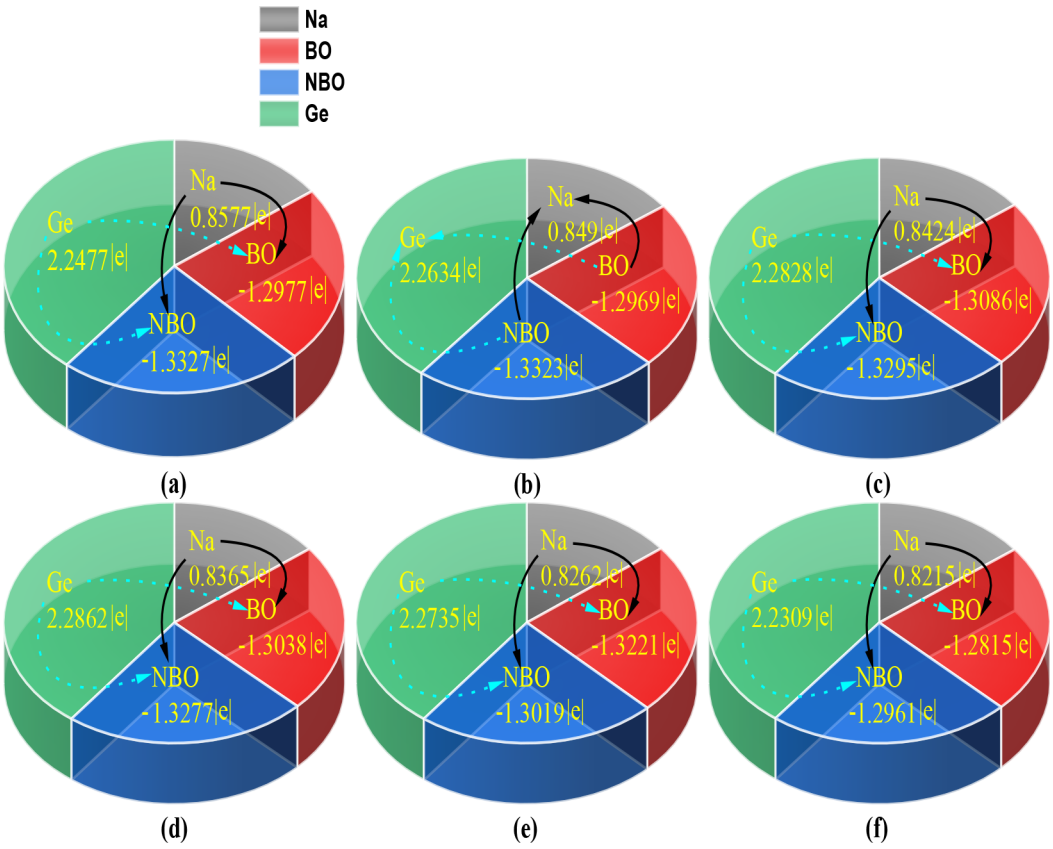

Figure 4. Bader charge transfer (relative to atoms) of Na_2GeO_3: (a) 0 GPa, (b) 5 GPa, (c) 10 GPa, (d) 15 GPa, (e) 20 GPa, and (f) 25 GPa.

the valence charge is very consistent even when the pressure escalates up to 25 GPa. On analyzing the valence charges of BO and NBO, the charges for NBO are larger than that of BO except at 20 GPa. That is simply due to the effect of structural phase transition observed at P ∼ 20 GPa where atomic and electronic structure rearrangements are possibly taking place. The Bader charge transfer analysis among the relative atoms is presented in Figure 4. The data reveal that charge transfer occurs primarily between the oxygen atom (both BO and NBO) and the sodium (Na) and germanium (Ge) atoms in Na_2GeO_3. From Figure 4 (a), we can find that both Na and Ge atoms dissipate ∼0.86 |e| and 2.25 |e| while BO and NBO accumulate ∼1.30 |e| and 1.33 |e| to form a stable structure. And therefore, the region near the Fermi level in the DOS plots for the valence band side is mostly contributed by the NBO, since charge accumulation by NBO is higher than BO. Also, Ge has transferred more charges than that of Na, consequently, the Ge atom is more dominant in the conduction region compared to Na.

Optical Properties. The study of the interaction between electromagnetic radiation and any materials can be interpreted from the optical properties. It is crucial for industrial as well as scientific applications in the fields of laser technology, mirror production, optical windows, photovoltaic devices, and many more.[52−54] In the current work, to examine the optical properties of Na_2GeO_3, we have calculated the optical dielectric constant (ϵ), absorption coefficient (α), and refractive index (η) under different compressive pressures. Since the observed results are most prominent along the x-axis, interpretation and analysis are done for the x-axis in this work. The frequency-dependent complex dielectric function (ω) is adopted to determine different optical parameters. Complex dielectric function is expressed as follows

$$\varepsilon = \varepsilon_1 + i\varepsilon_2 \tag{1}$$

Here, ϵ_1 and ϵ_2 are the real and imaginary parts of the dielectric constant, respectively. The above equation is interconnected with the electronic structures and gives the linear response of the studied material and electromagnetic radiations. The imaginary part (ϵ_2) is given as[55]

$$\varepsilon_2(\omega) = \frac{\hbar^2 e^2}{\pi m^2 \omega^2} \sum_{nn'} \int_k d^3k \left| \left\langle \vec{k}_n \middle| \vec{p} \middle| \vec{k}_n' \right\rangle \right|^2 \times [1 - f(\vec{k}_n)]\delta (E_{\vec{k}_n} - E_{\vec{k}_n'} - \hbar\omega) \tag{2}$$

where, $\vec{p}$ is the momentum operator, $|\vec{k}_n\rangle$ is the eigenfunction of the eigenvalue $E_{\vec{k}_n}$ and $f(\vec{k}_n)$ is the Fermi distribution function. For the real part (ϵ_1), the equation employed is

$$\varepsilon_1(\omega) = 1 + \frac{2}{\pi} \int_0^\infty \frac{\varepsilon_2(\omega')\omega' d\omega'}{\omega'^2 - \omega^2} \tag{3}$$

For extinction coefficient (κ), absorption coefficient (α), and refractive index (η), the formulas employed are given as

$$\kappa(\omega) = \sqrt{\frac{(\varepsilon_1^2 + \varepsilon_2^2)^{1/2} - \varepsilon_1}{2}} \tag{4}$$

$$\alpha(\omega) = \frac{2\omega\kappa(\omega)}{c} \tag{5}$$

https://doi.org/10.1021/acsomega.3c00499
ACS Omega 2023, 8, 16869−16882

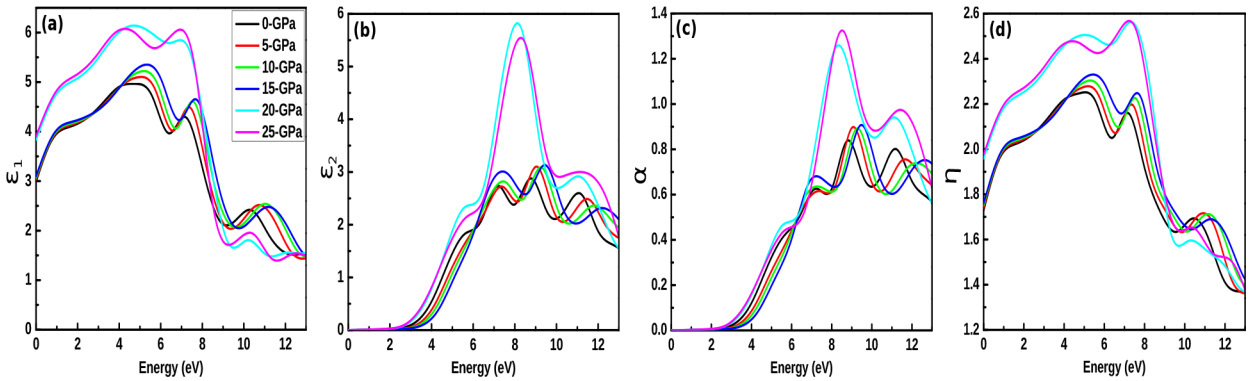

Figure 5. Optical parameters as a function of the photon energy (in eV) under 0, 5, 10, 15, 20, and 25 GPa pressures: (a) real part of dielectric function (ϵ_1), (b) imaginary part of dielectric function (ϵ_2), (c) absorption coefficient (α), and (d) refractive index (η).

Table 4. Calculated Elastic Constants C_{ij} under Different Compressive Pressures (in GPa units)[a]

P	C_{11}	C_{22}	C_{33}	C_{44}	C_{55}	C_{66}	C_{12}	C_{13}	C_{21}	C_{23}	C_{31}	C_{32}
0	110.81	89.87	88.45	47.23	36.37	32.37	33.43	20.34	33.43	34.40	20.34	34.40
5	144.09	116.87	111.41	47.99	40.26	33.43	61.75	34.33	61.75	43.24	34.33	43.24
10	168.04	133.25	128.07	50.48	41.49	32.83	100.79	50.58	100.79	49.08	50.58	49.08
15	195.15	151.54	159.86	52.11	46.10	19.15	138.63	67.25	138.63	67.21	67.25	67.21
20	439.08	126.60	183.95	45.25	65.69	65.81	95.69	86.22	95.69	38.13	86.22	38.13
25	496.03	157.52	209.44	54.29	71.32	73.34	104.62	101.03	104.62	42.98	101.03	42.98

[a]Here in this table, at 0−15 GPa Na_2GeO_3 is in the orthorhombic phase, and at 20 and 25 GPa Na_2GeO_3 is in the tetragonal phase.

$$\eta(\omega) = \sqrt{\frac{(\epsilon_1^2 + \epsilon_2^2)^{1/2} + \epsilon_1}{2}} \quad (6)$$

In Figure 5 (a) and (b), plots for ϵ_1 and ϵ_2 under different compressive pressures are presented. For ϵ_1, we observed two prominent peaks. The first peaks are within the range of 4−5.5 eV photon energy, while the second peaks are within 7−8 eV for each applied pressures. For ϵ_2, the most active regions are within the range of 5−10 eV photon energy. Within this region, one can find three prominent peaks for P = 0 to 15 GPa, while only one prominent peak is observable for P = 20 and 25 GPa. Moreover, for both ϵ_1 and ϵ_2, the dielectric constant spectra peaks have shown a blue shift with a slightly increasing magnitude of the dielectric constant values as the pressure escalates up to 15 GPa. Conversely, a red shifting of ϵ_2 is observed for 20 and 25 GPa leading to enhancement in the optical properties. A similar spectral behavior is observed for Figure 5 (c) and (d) as the parameters such as α and η are in close relation with the complex dielectric constants ϵ_2 and ϵ_1, respectively. The reason that enhanced optical behavior are observed at 20 and 25 GPa is due to the fact that at such pressures, the studied system undergoes direct band electronic transition from the indirect characteristics. Therefore, no change in momentum is required for an electron in the conduction band to recombine with a hole in the valence band. Thus, at 20 and 25 GPa, the optical parameters that have been presented in terms of photon energy (eV) were enhanced as compared to P = 0−15 GPa. Similarly, pressure-dependent enhancement of optical properties was formerly reported for halide perovskite, sulvanite compounds, and glass materials.[56−60] However, compared to these compounds, Na_2GeO_3 has shown better enhancement due to the resultant direct band electronic transition at $P \sim 20$ GPa.

Our main concern is to observe the variation of absorption spectra under the applied pressure for its potential application in optoelectronic devices. Here, we have calculated the absorption coefficient (α) as a function of incident photon energy under different compressive isotropic pressures, as shown in Figure 5 (c). Interestingly, the absorption spectra fall within the Vis−UV range, and the active regions have started from 2.8 eV photon energy which is comparable to Na_2SiO_3.[35] Referring to the black line (i.e., 0-GPa) of Figure 5 (c), the minimum threshold energy is found to be 3.2 eV which corresponds to an optical band gap and is in good agreement with the first direct electron transition from the top of the valence band (O-p) to the bottom of the conduction band (Ge-p) along Γ-symmetry. We have observed three prominent peaks at 7.2 9, and 11.2 eV. The first peak at 7.2 eV is the result of the transition from the first band of the valence region and the third band of the conduction region along *Z*-symmetry. The second peak at 9 eV is the probability transition from the 11th band of the valence region to the fourth band of the conduction region along *Y*-symmetry. The third peak at 11.1 eV is due to the outcome of the transition from the 14th band of the valence region (∼−3.3 eV) and the fifth band of the conduction region (∼7.9 eV) along *S*-symmetry. Moreover, between 0 and 15 GPa, the prominent peaks of the absorption spectra show a blue shift up to 15 GPa, but at 20 GPa, we observed highly anisotropic behavior and the peak is red-shifted with largely increasing absorption intensity. The discrepancy at 20 and 25 GPa is due to the experience of large tensile strain along the *x*-axis when the applied compressive pressure escalates from 15 to 20 GPa. The same effect can be observed for the refractive index (η) plot (see Figure 5 (d)). From the spectral plot of η it is comprehensible that the static refractive index $\eta(0)$ for 0−15 GPa are within 1.7−1.8, while at 20 and 25 GPa, $\eta(0)$ are ∼1.96 and 1.97, respectively. The obtained refractive indices are in good agreement with the experimental investigation led by Jin et al.[61] where the reported refractive indices were: η = 1.62 for 1.2 mol % of Na_2O and 98.8 mol % of GeO_2 while η = 1.69 for

https://doi.org/10.1021/acsomega.3c00499
ACS Omega 2023, 8, 16869−16882

Table 5. Calculated Elastic Moduli (Bulk Modulus (B), Young's Modulus (Y), and Shear Modulus (G), All in GPa Units) and Poisson's Ratio (ν) (Unitless) under Different Unidirectional Pressures (in GPa units)[a]

P	B_V	B_R	B_H	Y_V	Y_R	Y_H	G_V	G_R	G_H	ν_V	ν_R	ν_H
0	51.72	51.36	51.54	88.83	85.86	87.34	36.59	35.15	35.87	0.2137	0.2214	0.2175
5	72.34	70.72	71.53	101.05	97.81	99.43	39.87	38.52	39.20	0.2672	0.2695	0.2683
10	92.25	87.42	89.83	105.35	96.64	101.00	40.22	36.73	38.47	0.3097	0.3157	0.3126
15	116.97	110.70	113.83	105.39	80.34	92.86	39.04	29.13	34.08	0.3498	0.3790	0.3639
20	132.19	93.19	112.69	179.91	149.16	164.53	70.65	60.48	65.56	0.2732	0.2332	0.2563
25	151.14	110.68	130.91	205.62	174.54	190.08	80.75	70.54	75.64	0.2733	0.2372	0.2577

[a]Here in this table, the subscripts V, R, and H represent Voigt, Reuss, and Hill assumptions respectively.

Table 6. Calculated Pugh's Ratio (k) (Unitless), Velocity of Sound Calculated from Hill Moduli under Different Pressures (in Km/s), Melting Temperature (T_m), Kleinman Coefficient (ζ), and Vickers Hardness (H)[a]

P	k_V	k_R	k_H	v_t	v_l	v_{av}	ζ	A_{an}	H_V	H_R	H_H	T_m
0	1.41	1.46	1.44	3.35	5.58	3.71	0.45	2.80	7.96	7.30	7.63	1207.99 ± 300
5	1.81	1.84	1.83	3.49	6.19	3.88	0.56	3.08	5.61	5.31	5.46	1404.72 ± 300
10	2.29	2.38	2.33	3.42	6.55	3.83	0.71	3.45	3.57	2.97	3.27	1546.28 ± 300
15	2.99	3.80	3.34	3.17	6.86	3.57	0.79	3.54	1.73	0.02	0.84	1706.53 ± 300
20	1.87	1.54	1.72	4.21	7.36	4.68	0.37	3.90	8.60	10.29	9.26	3148.40 ± 300
25	1.87	1.57	1.73	4.45	7.78	4.94	0.36	3.94	9.54	11.54	10.23	3485.03 ± 300

[a]Here in this table, the subscripts t, l, and av represent transverse, longitudinal, and average velocities, respectively.

14.95 mol % of Na_2O and 85.05 mol % of GeO_2. This reveals that the studied system Na_2GeO_3 is either a transparent or translucent-like compound in nature. However, as compared to Na_2SiO_3, the system being studied has a higher static refractive index, where the reported static refractive index for Na_2SiO_3 at 0 GPa was $\eta(0) = 1.03$ along x-axis.[35]

Mechanical Properties. In this section, we will focus on the mechanical properties of Na_2GeO_3 under different compressive pressures to perceive the applicability of the studied compound to practical appliances. In this regard, we have calculated the elastic constants (C_{ij}) as shown in Table 4 and other mechanical properties as shown in Tables 5 and 6. The structural investigation shows that Na_2GeO_3 exists as an orthorhombic phase between 0 and 15 GPa and a tetragonal phase at 20 and 25 GPa. The mechanical stabilities at these two phases are checked by employing the necessary and sufficient Born criteria for orthorhombic and tetragonal systems, given as[62−64]

$$C_{11} > 0,\ C_{11}C_{22} > C_{12}^2,\ [C_{11}C_{22}C_{33} + 2C_{12}C_{13}C_{23} - C_{11}C_{23}^2 - C_{22}C_{13}^2 - C_{33}C_{12}^2] > 0,\ C_{44} > 0,\ C_{55} > 0,\ C_{66} > 0 \quad (7)$$

$$C_{11},\ C_{33},\ C_{44},\ C_{66} > 0,\ C_{11} - C_{12} > 0,\ C_{11} + C_{33} - 2C_{13} > 0,2C_{11} + C_{33} + 2C_{12} + 4C_{13} > 0 \quad (8)$$

respectively, and we observed that both these phases show mechanical stabilities.

From Table 4, we can find that the calculated C_{11}, C_{22}, and C_{33} are considerably larger than C_{44}, C_{55}, and C_{66}. This implies that the compound being investigated has more resistance to axial compression as compared to shear deformation, which is further confirmed by showing that the bulk modulus (B) is greater than the shear modulus (G) (see Table 5). The large values of C_{11}, C_{22}, and C_{33} as compared to other elastic constants also suggest that Na_2GeO_3 shows highly anisotropic single-crystal elasticity behavior. For investigating the internal deformation stability, we have calculated the Kleinman coefficient (ζ) using the equation given as[65]

$$\zeta = \frac{C_{11} + 8C_{12}}{7C_{11} + 2C_{12}} \quad (9)$$

The Kleinman coefficient ζ which is in the range $0 \le \zeta \le 1$ determines the stability of the compound against stretching and bending. A closer value of ζ to 0 indicates a negligible contribution of bond bending to resist the applied pressures. From the calculation values given in Table 6, it is possible to state that the mechanical strength of the studied compound due to the contribution from bond bending increases with pressure as pressure escalates from 0 to 15 GPa. On the other hand, at 20 and 25 GPa (i.e., after the structural phase transition to tetragonal from orthorhombic phase) the internal deformation stability is highly due to the bond stretching. For the practical application of any materials, knowledge of the melting temperature is highly needed. In this regard, we have calculated the melting temperature (T_m) of Na_2GeO_2 under different applied pressures by employing the equation given as[66,67]

$$T_m = 553 + 5.911C_{11} \pm 300 \quad (10)$$

The calculated T_m at $P = 0$ GPa is higher than that of Na_2SiO_3 where the experimentally reported melting point was 820 °C.[68] The calculated T_m shown in Table 6 reveals that the melting temperature increases with applied pressures. However, one can find that between $P = 0$−15 GPa the rise on T_m with P is very regular, but once P reaches 20 GPa, T_m surges to ∼2875 °C. This implies that the tetragonal phase of Na_2GeO_3 is more applicable at a higher temperature than that of the orthorhombic phase.

In Table 5, the calculated elastic moduli such as bulk modulus (B), Young's modulus (Y), shear modulus (G), and Poisson's ratio which are estimated in terms of Voigt, Reuss, and Hill assumptions are presented.[69−71] The calculated bulk modulus that can be used to estimate the incompressibility of studied materials under applied pressure reveals that the ability to withstand changes in volume increases as the applied

https://doi.org/10.1021/acsomega.3c00499
ACS Omega 2023, 8, 16869−16882

pressure is increasing. Also, the observed Young's modulus that determines the resistance of solid materials to deformation shows that Y values are higher than 90 GPa at each applied pressure. This implies that the compound being investigated is a stiff material which is very much needed for practical applications since stiff compounds do not bend or change shape easily.[72] The lower obtained values of shear modulus as compared to B and Y at each pressure indicate that the applied pressures are less effective in deformation along the plane of the direction of applied pressure. To understand the brittleness or ductility of the studied system, we also perform the calculations for Poisson's ratio (ν) and Pugh's ratio (k) under different applied pressure (see Tables 5 and 6). Clearly, between 0 and 15 GPa, ν and k increase with applied pressure. However, at 20 GPa it becomes less ductile as ν and k are decreasing. From this result, it is possible to state that the orthorhombic phase of Na_2GeO_3 has better ductility compared to its tetragonal phase. From certain reviewed literature, it is well-known that in crystallophysics isotropy/anisotropy plays an important role. Therefore, the elastic anisotropic factor (A_{an}) is calculated using the equation given as[73−75]

$$A_{an} = \frac{4C_{11}}{C_{11} + C_{33} - 2C_{13}} \tag{11}$$

From A_{an} values given in Table 6 it has been understood that the compound being investigated is highly anisotropic in nature (for isotropic materials, $A_{an} = 1$). Also, as applied pressures increase, the studied system has shown a more anisotropic behavior. Herein, the calculation for Vickers hardness (H) given by the equation[76]

$$H = 2\left[\left(\frac{G}{B}\right)^2 G\right]^{0.585} - 3 \tag{12}$$

From the calculated values of H, it is clear that between P = 0−15 GPa the hardness reduces with increasing pressure and reaches a minimum value of H = 0.84 GPa at P = 15 GPa.[77] However, as applied pressure is further increased, the value of H shoots up rapidly and extends even up to H = 10.23 GPa at P = 25 GPa. Overall, it is possible to state that the tetragonal phase of Na_2GeO_3 has higher H values as compared to its orthorhombic phase. One of our main concerns for mechanical properties calculation is to figure out the average sound velocity (v_{av}) determine by both transverse and longitudinal velocities (v_t and v_l) calculated by the equation given as[78−80]

$$v_{av} = \left[\frac{1}{3}\left(\frac{1}{v_l^3} + \frac{2}{v_t^3}\right)\right]^{-1/3} \tag{13}$$

where, $v_l = \sqrt{\frac{3B + 4G}{3\rho}}$ and $v_t = \sqrt{\frac{G}{\rho}}$. Here, ρ is the density.

From our calculation for the velocity of sound at different pressures (see Table 6), we can find that at P = 20 GPa the values of v_t, v_l, and v_{av} increase rapidly. This suggests that after phase transition the density of Na_2GeO_3 increases largely (i.e., the tetragonal phase of Na_2GeO_3 has a higher density as compared to orthorhombic phase), which leads to more elasticity in the medium and hence the ease by which compression and rarefaction can take place.

Piezoelectric Properties. Wide band gap semiconductors possess some critical advantages including a better ability to tune the efficiency for some practical purposes by making use of band gap engineering.[81,82] Since glass-like materials usually have wide band gaps and own high mechanical stabilities, such compounds give superior piezoelectric responses. It is mandatory that piezoelectric materials are an insulator or semiconductor with a sufficiently wide band gap to avoid current leakage. The applicability of piezoelectric materials for actuators, sensors, and monitoring heartbeats and breathing, etc. has made these materials a fascinating topic among researchers.[83−86] In this section, we report direct piezoelectric constants for Na_2GeO_3 under different applied pressures, presented in terms of electronic "clamped ion" and total "relaxed ion", including both ionic and electronic contributions. The piezoelectric tensors are calculated with the modern theory of polarization based on the Berry phase approximation where the third-rank piezoelectric tensors $e_{i\nu}$ represent the correlation between the polarization tensor P_i and the second-rank strain tensor η_ν.[87]

$$e_{i\nu} = \frac{\delta P_i}{\delta \eta_\nu} \tag{14}$$

where, $i = x, y, z$ and $\nu = xx, yy, zz, yz, xz$, and xy.

For clamped ion piezoelectric constant, the formula employed is given as

$$e_{i\nu} = \frac{\delta \sigma_\nu}{\delta \varepsilon_i} \tag{15}$$

where σ is the stress tensor and ε is the constant electric field.

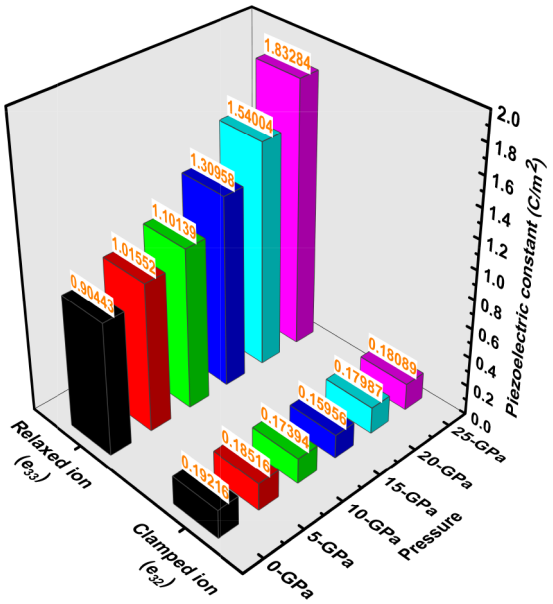

Figure 6. Maximum direct piezoelectric constant is given in terms of relaxed and clamped ions under varying applied compressive pressures. For the relaxed ion and clamped ion, maximum piezoelectric constants are obtained at e_{33} and e_{32}, respectively.

As shown in Figure 6 and Table 7, the maximum piezoelectric constants for relaxed ion and clamped ion are along $e_{33} \equiv e_{zzz}$,i.e., piezoelectric response along the z-direction due to strain η_{zz} and $e_{32} \equiv e_{zyy}$, i.e., response along z due to strain η_{yy}, respectively. On analyzing the variation of maximum total piezoelectric constants as a function of applied pressures, one can find that the values of e_{33} increase with increasing pressure, and at 20 GPa, the rate of increasing the constant

https://doi.org/10.1021/acsomega.3c00499
ACS Omega 2023, 8, 16869−16882

Table 7. Calculated Piezoelectricity and Electronic "Clamped Ion" and Total "Relaxed Ion" Constants under Different Compressive Pressure[a]

P		e_{11}	e_{32}	e_{33}	e_{25}	e_{16}
0	Clamped	0.0834	0.1922	−0.2921	0.1130	0.0611
	Relaxed	−0.1808	−0.2245	0.9044	−0.0478	−0.0909
5	Clamped	0.0852	0.1852	−0.2772	0.0959	0.0581
	Relaxed	−0.1664	−0.2303	1.0155	−0.0939	−0.1075
10	Clamped	0.0852	0.1739	−0.2587	0.0819	0.0528
	Relaxed	−0.1571	−0.2310	1.1014	−0.1100	−0.1031
15	Clamped	0.0848	0.1596	−0.2332	0.0733	0.0512
	Relaxed	−0.1436	−0.2257	1.3096	−0.1229	−0.1002
20	Clamped	0.1388	0.1799	−0.2717	0.1544	0.0724
	Relaxed	−0.4338	−0.1267	1.5400	0.0711	−0.0964
25	Clamped	0.1289	0.1809	−0.2431	0.1670	0.0690
	Relaxed	−0.4702	−0.0944	1.8328	0.1525	−0.0821

[a]Here, the piezoelectric constants are in units of C/m^2.

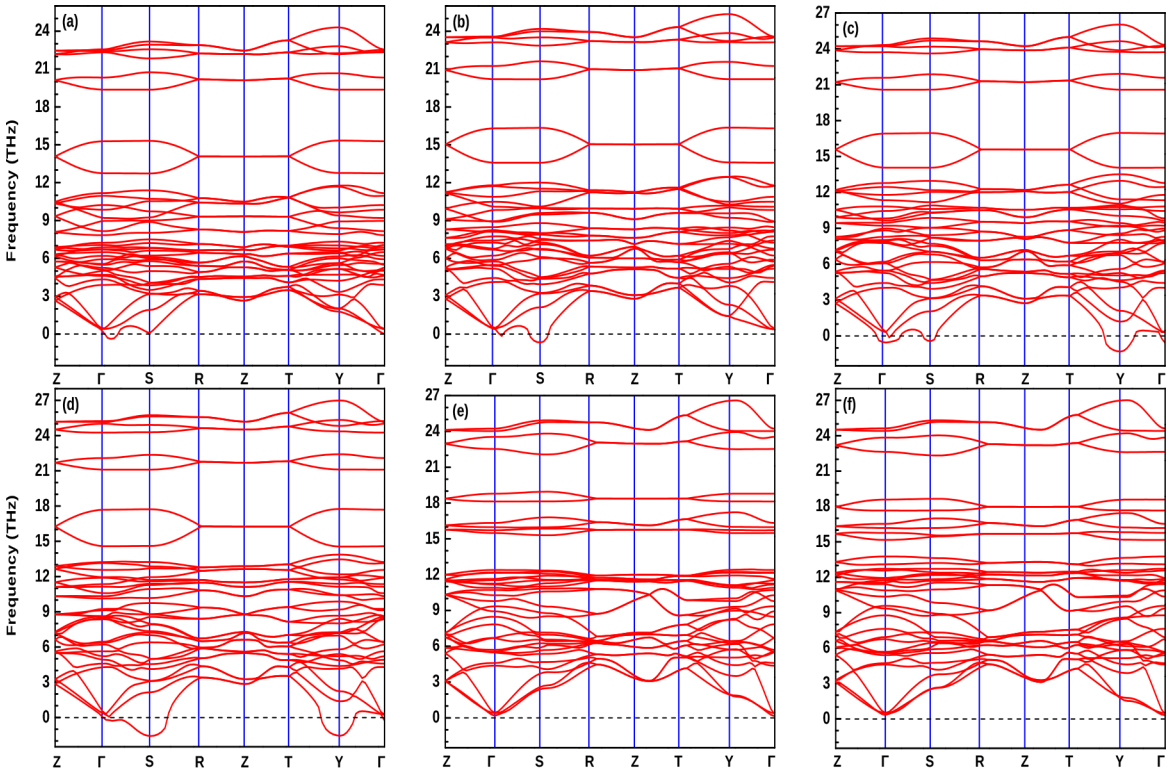

Figure 7. Phonon dispersion curve for Na_2GeO_3 at (a) 0 GPa, (b) 5 GPa, (c) 10 GPa, (d) 15 GPa, (e) 20 GPa, and (f) 25 GPa.

values (i.e., e_{33}) is enhanced. This reveals that the tetragonal phase of Na_2GeO_3 has better piezoelectric responses compared to its orthorhombic phase. The fact that with the application of pressure the piezoelectric constants are varying shows that the piezoelectricity is significantly affected by the motion of the constituent atoms. Our calculated e_{ij} are higher than standard piezoelectric materials; α quartz whose reported values were e_{11} = 0.15 C/m^2 and 0.07 C/m^2 at room temperature and at 5 K, respectively.[88] However, compared to some ferroelectric materials such as $SrTiO_3$ that show the piezoelectric response of e_{33} = 8.82 C/m^2, our calculated values are fairly low.[89] Therefore, more rigorous research to enhance its piezoelectricity is needed in order to utilize this compound for practical piezoelectric devices. In Table 7, we report the clamped ion and relaxed ion piezoelectric constants. The fact that we are observing a change of sign between the clamped ion and relaxed ion under different applied pressures reveals a large effect of nuclear relaxation. However, above 20 GPa, e_{25} values for clamped and relaxed ions do not experience a change of sign, and this shows that the compound being investigated is stiffer at higher pressure. Therefore, a slight increase in applied external pressure has a large effect on its piezoelectric responses.

Thermodynamical Properties. To investigate the thermodynamic properties, we first calculate the phonon dispersion curves along the high-symmetry direction for the different applied pressures, as shown in Figure 7. Since the considered system consists of 12 atoms in the unit cell, there are 36 branches in the phonon dispersion curves. It has been clearly seen that the calculated phonon dispersion curve display softening behavior, and therefore, a small negative phonon frequency (f < −1 THz) is observed near the Γ-

https://doi.org/10.1021/acsomega.3c00499
ACS Omega 2023, 8, 16869−16882

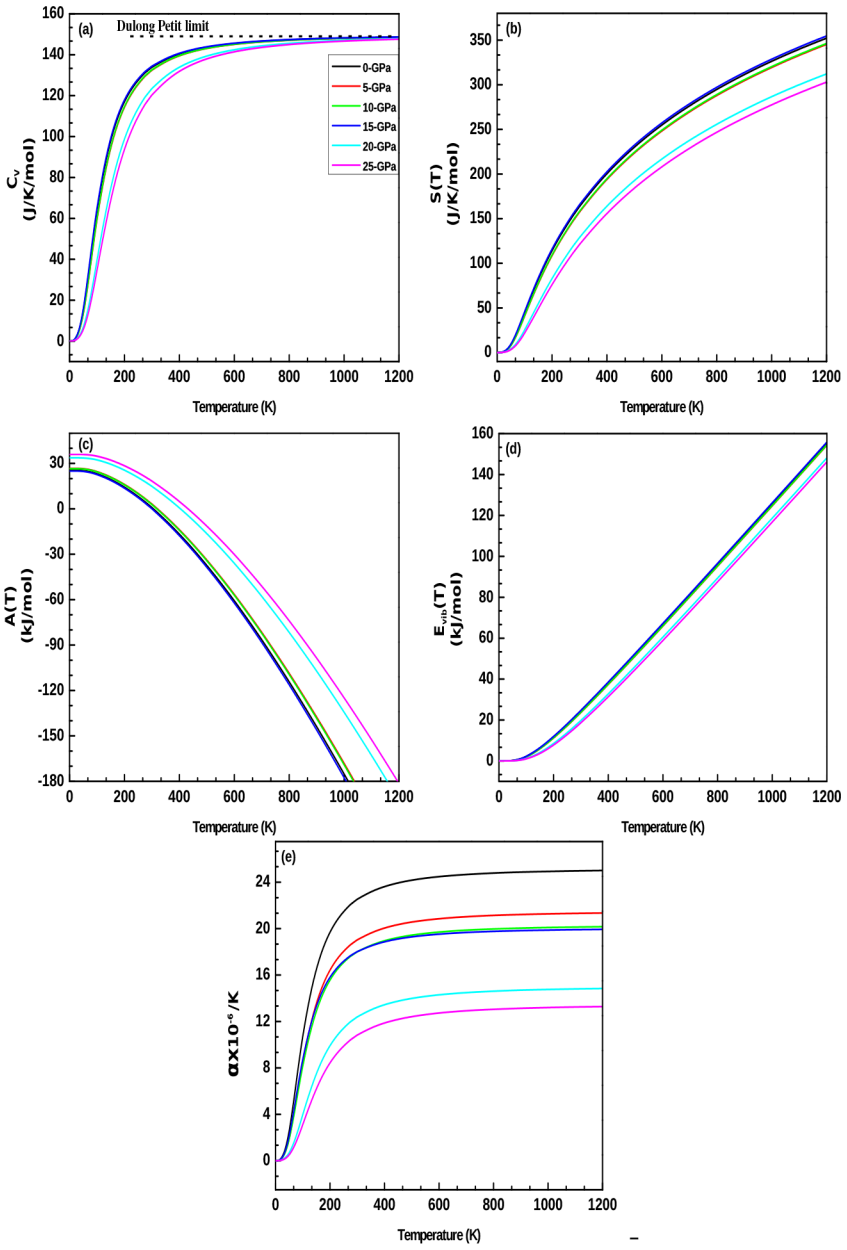

Figure 8. Dependencies of (a) constant-volume heat capacity C_v, (b) vibrational entropy $S(T)$, (c) vibrational Helmholtz free energy $A(T)$, (d) change in vibrational internal energy $E_{vib}(T)$, and (e) linear thermal expansion coefficient α on temperature at various applied pressures.

symmetry for P = 0 GPa, which could be numerical noise while performing the calculation. This implies that the pristine state of Na_2GeO_3 is dynamically stable. However, as the applied pressure is increasing, higher negative phonon frequencies are displayed along Γ, S, and Y symmetry for P = 5, 10, and 15 GPa (see Figure 7 (b)−(d)). This indicates that at such pressures the considered system is dynamically unstable. The negative phonon frequencies that appears when the applied external pressure increases implies the studied system undergo a change in structural and atomic rearrangement and a possibility of the occurrence of phase transition to a lower symmetry. Interestingly, at P = 20 and 25 GPa (where structural phase transition is observed), the studied system is dynamically stable, suggesting that for Na_2GeO_3 the next stable structural phase, i.e., from orthorhombic → tetragonal phase, can be achieved by applying $P \sim 20$ GPa. As seen from the phonon dispersion curve for each different applied pressure, within the higher frequency optical phonon region there is a gap between the optical−optical phonon modes. This gap is due to the difference in mass between Na, Ge, and O atoms. At P = 0−15 GPa, the nature of optical phonons within the higher frequency regions is very regular while some changes are clearly seen for P = 20 and 25 GPa, suggesting the structural and atomic rearrangement above $P \sim 20$ GPa.

The main concern for the study of thermodynamic properties is the understanding of vibrational properties such as heat capacity C_v, entropy S(T), Helmholtz free energy A(T), change in internal energy E_{vib}(T), and linear thermal expansion coefficient α as a function of temperature at various pressures, as shown in Figure 8. In this study, the quasiharmonic Debye model is used to predict the thermodynamic properties.[90] According to this model, we have

https://doi.org/10.1021/acsomega.3c00499
ACS Omega 2023, 8, 16869−16882

$$\Theta = \frac{h}{k}\left(\frac{3nN_A\rho}{4\pi M}\right)^{1/3} v_{av} \quad (16)$$

$$C_v = 3nk\left[4D\left(\frac{\Theta}{T}\right) - \frac{3\Theta/T}{e^{\Theta/T} - 1}\right] \quad (17)$$

$$S(T) = nk\left[4D\left(\frac{\Theta}{T}\right) - 3\ln(1 - e^{-\Theta/T})\right] \quad (18)$$

$$A(T) = nkT\left[\frac{9}{8}\frac{\Theta}{T} + 3\ln(1 - e^{-\Theta/T}) - D(\Theta/T)\right] \quad (19)$$

$$\alpha = \frac{\gamma C_v}{B_T V} \quad (20)$$

Here, h is Planck's constant, n number of atoms per formula unit, N_A Avogadro's number, ρ density, M molecular mass, k Boltzmann constant, Θ Debye temperature, T temperature, γ Grueneisen parameter, B bulk modulus, V volume, E_T the electronic plus vibrational energy of formation, and D the Debye integral defined as

$$D(y) = \frac{3}{y^3}\int_0^y \frac{x^3}{e^x - 1}\,dx \quad (21)$$

In thermodynamics and statistical studies, heat capacity plays an important parameter to investigate the lattice vibration characteristics. The nature of heat capacity (C_v) curves as shown in Figure 8 (a) can be broadly divided into two parts to discuss; first, when $T \ll \Theta$, the curve follows the rule given as

$$C_v = \frac{12}{5}\pi^4 nR\left(\frac{T}{\Theta}\right)^3 \quad (22)$$

where R is the universal gas constant. Second, if $T \gg \Theta$, the rule of the C_v curve is

$$C_v \simeq 3nR \quad (23)$$

From the C_v plot, we can see that the C_v curves for all applied pressures obey the two rules mentioned above. At $T \ll \Theta$ (values for Θ at 0 K are given in Table 8), the increase in C_v is proportional to T^3, which confirms that our calculation follows Debye's low-temperature-specific heat law. However, C_v are almost constant for each different pressure when $T \gg \Theta$; i.e., C_v tends to the Dulong–Petit limit. This shows that, at high temperature, our calculation obeys the classical thermodynamics of the Dulong–Petit law. Between 0 and 15 GPa, the plotted C_v curves are almost along the same line; this indicates heat capacity for orthorhombic phases of Na_2GeO_3 are almost fixed. However, red and green lines (i.e., C_v for 5 and 10 GPa) have slightly lower heat capacity values than black and blue lines (i.e., C_v for 0 and 15 GPa), which could be due to lower Θ values of the former two lines compared to the latter. On the other hand, comparing C_v values for P = 20 and 25 GPa with respect to those lower pressure, it can be noticed that heat capacity reduces at higher pressure. This shows that the orthorhombic phase of Na_2GeO_3 has better stability toward a change in temperature as compared to its tetragonal phase. From Figure 8 (b), when the change of entropy is analyzed within the temperature values ranging from 0 to 1200 K, the entropy value increases as the temperature increases. The rate of increase of entropy at lower temperature values is fast, while this rate of increasing is gradually reduces toward the high temperature values for each different applied pressures. However, for P = 20 and 25 GPa, the obtained entropy values are almost 6/7 times lower than those entropy values at lower pressures (P = 0, 5, 10, 15 GPa). This reveals that the orthorhombic phase has higher disorder or randomness than the tetragonal phase since thermal energy that is unavailable for doing useful work is higher for the orthorhombic phase of Na_2GeO_3. For P = 0 GPa at T = 300 K, C_v = 133.9 J/K/mol and S = 163.5 J/K/mol which are higher than silicate glass (Na_2SiO_3) reported by Belmonte et al.[91] where the estimated values were C_v = 109.5 J/K/mol and S = 112.5 J/K/mol at T = 300 K. This reveals that Na_2GeO_3 has better thermal stability as compared to Na_2SiO_3.

In Figure 8 (c), it is clearly seen that the vibrational Helmholtz free energy A(T) reduces with increasing temperature for each applied pressures. Comparing the orthorhombic phase of Na_2GeO_3 with its tetragonal phase, it is possible to notice that the thermodynamic potential (thermal energy) available for doing useful work is higher for the tetragonal phase. In Figure 8 (d) and (e), plots of change in vibrational internal energy E_{vib}(T) = E(T) − E_0, where E(T) is the vibrational energy of formation and E_0 is the zero point energy (calculated E_0 for each different pressures are given in Table 8) and linear thermal expansion coefficient α are presented. From Figure 8 (d), it is possible to state that E_{vib}(T) increases with increasing temperature, and the trend followed by each curve for different applied pressures is more or less similar to Figure 8 (a)–(c). The Gruneisen parameter (γ)[92] that correctly predicts the anharmonic properties of the solid material, such as thermal expansion effect, is given in Table 8. Values of γ initially increase with pressure and then drastically reduce when the studied compound undergoes structural phase transition. The coefficient of thermal expansion (α) is basically the change in strain due to change in temperature and is in close relation to the Young's modulus estimated in Voigt (uniform strain assumption). From Figure 8 (e), we can find that values of α shoot up rapidly when the temperature is below room temperature. α reduces as applied pressures are increasing, and the variation of the α curves for each different applied pressure at higher temperature region are in close comparable with variation of Y_v values (Y_v are given in Table 5). On analyzing the path followed by each curves, it is possible to state that when the pressure is increasing the compound becomes more stiff. However, between P = 0–15 GPa, the increment for which the stiffness is increasing reduces when the pressure escalates, and a large variation is not seen between the green and blue curves of Figure 8 (e) (i.e., for P = 10 and 15 GPa). In conclusion, it is possible to interpret that the tetragonal phase is stiffer even for certain high temperature

Table 8. Calculated Debye Temperature (Θ) (K), Grueneisen Parameter (γ) (Unitless), and Zero-Point Energy (E_0) (kJ/mol) for Na_2GeO_3 for Different Applied Pressures at 0 K

P	Θ	γ	E_0
0	453.2	1.36	25.43
5	475.8	1.59	26.70
10	472.5	1.85	26.52
15	445.6	2.25	25.01
20	600.8	1.53	33.72
25	641.6	1.54	36.01

https://doi.org/10.1021/acsomega.3c00499
ACS Omega 2023, 8, 16869–16882

range than its orthorhombic phase since α is lower for the tetragonal phase of Na_2GeO_3. For Na_2GeO_3 at P = 0 GPa and T = 300 K, the calculated $\alpha = 2.25 \times 10^{-5}$ K^{-1}. However, for $(Na_2O)_x(SiO_2)_{1-x}$ the theoretical work (α_t) of Subedi et al.[48] and experimental work (α_e) of White et al.[93] reveal that at T = 283 K, for x = 0.3, the $\alpha_t(\alpha_e) = 0.9 \times 10^{-5}(1.2 \times 10^{-5})$ K^{-1}. This shows that upon heating the sodium germanate glass will expand more as compared to sodium silicate glass due to a higher value of α.

CONCLUSIONS

In summary, we report the results of the variation of the structural, electronics, optical, mechanical, piezoelectric, and thermodynamic properties of a complex glasslike Na_2GeO_3 under compressive pressure as investigated from DFT method. We have observed a structural phase transition from orthorhombic to tetragonal (highly sensitive to pressure) at ∼20 GPa. We have also observed a band gap fluctuation on increasing the applied pressure, which enable tuning of band gap for optical absorption. A band gap flip from indirect to direct occurs at ∼20 GPa. Both mechanical and thermodynamical stabilities are verified by fulfilling the necessary and sufficient Born criteria. Furthermore, the thermodynamical stability has been confirmed by calculating the phonon dispersion curves for each pressure. The study of thermodynamic properties had shown that the thermal energy needed for doing useful work was higher for the orthorhombic phase than the tetragonal phase, which infers the high linear thermal expansion coefficient of orthorhombic phase. The orthorhombic phase had lost more properties than its tetragonal phase at a higher temperature. From the computed piezoelectric tensor (both in relaxed and clamped ions), it has been confirmed that Na_2GeO_3 could be a potential material for future piezoelectric devices. The present research on Na_2GeO_3 may provide a direction for developing a new sensors and piezoelectric device with outstanding mechanical and thermal stabilities.

ASSOCIATED CONTENT

Supporting Information

The Supporting Information is available free of charge at https://pubs.acs.org/doi/10.1021/acsomega.3c00499.

Table S1: Optimized final position of atoms at different pressure given in fractional coordinates (PDF)

AUTHOR INFORMATION

Corresponding Author

Dibya Prakash Rai − *Physical Sciences Research Center (PSRC), Department of Physics, Pachhunga University College, Mizoram University, Aizawl 796001, India;* orcid.org/0000-0002-3803-8923; Email: dibyaprakashrai@gmail.com

Authors

Zosiamliana Renthlei − *Physical Sciences Research Center (PSRC), Department of Physics, Pachhunga University College, Mizoram University, Aizawl 796001, India; Department of Physics, Mizoram University, Aizawl 796009, India*

Mattipally Prasad − *Department of Physics, University College of Science, Osmania University, Hyderabad, Telangana 500007, India*

Juluru Sivakumar − *Department of Physics, University College of Science, Osmania University, Hyderabad, Telangana 500007, India*

Lalhriat Zuala − *Physical Sciences Research Center (PSRC), Department of Physics, Pachhunga University College, Mizoram University, Aizawl 796001, India*

Lalrinthara Pachuau − *Physical Sciences Research Center (PSRC), Department of Physics, Pachhunga University College, Mizoram University, Aizawl 796001, India*

Yengkhom Rangeela Devi − *Physical Sciences Research Center (PSRC), Department of Physics, Pachhunga University College, Mizoram University, Aizawl 796001, India*

Ningthoujam Surajkumar Singh − *Physical Sciences Research Center (PSRC), Department of Physics, Pachhunga University College, Mizoram University, Aizawl 796001, India*

Gulmurza Abdurakhmanov − *National University of Uzbekistan, 100174 Tashkent, Uzbekistan*

Amel Laref − *Department of Physics and Astronomy, College of Science, King Saud University, Riyadh 11451, Saudi Arabia*

Complete contact information is available at: https://pubs.acs.org/10.1021/acsomega.3c00499

Notes

The authors declare no competing financial interest.

ACKNOWLEDGMENTS

D. P. Rai acknowledges the Government of India, Ministry of Science and Technology, Department of Science & Technology (International Bilateral Cooperation Division) for supporting the Indo−Uzbek joint project via Sanction No. INT/UZBEK/P-02. G. Abdurakhmanov acknowledges the Government of Uzbekistan and Ministry of Innovative Development for supporting the Uzbekistan−India joint grant Uzb-Ind-20221-78. Also, Amel Laref acknowledges support from the "Research Center of the Female Scientific and Medical Colleges" Deanship of Scientific Research, King Saud University, Riyadh, Saudi Arabia.

REFERENCES

(1) Marrocchelli, D.; Salanne, M.; Madden, P. A. High-pressure behaviour of GeO 2: a simulation study. *J. Phys.: Condens. Matter* **2010**, *22*, 152102.

(2) Li, N.; Sakidja, R.; Aryal, S.; Ching, W.-Y. Densification of a continuous random network model of amorphous SiO 2 glass. *Phys. Chem. Chem. Phys.* **2014**, *16*, 1500−1514.

(3) Milman, V.; Perlov, A.; Refson, K.; Clark, S. J.; Gavartin, J.; Winkler, B. Structural, electronic and vibrational properties of tetragonal zirconia under pressure: a density functional theory study. *J. Phys.: Condens. Matter* **2009**, *21*, 485404.

(4) Holomb, R.; Mitsa, V.; Akyuz, S.; Akalin, E. New ring-like models and ab initio DFT study of the medium-range structures, energy and electronic properties of GeSe 2 glass. *Philos. Mag.* **2013**, *93*, 2549−2562.

(5) Gong, H.; Song, B.; Yang, Y.; Wang, P.; Cao, Z.; Chen, X.; Zhao, G.; Peng, S.; Liu, Y.; Han, G. Ab initio molecular dynamics simulation of the structural and electronic properties of aluminoborosilicate glass. *J. Am. Ceram. Soc.* **2021**, *104*, 3198−3211.

(6) Biskri, Z. E.; Rached, H.; Bouchear, M.; Rached, D. Computational study of structural, elastic and electronic properties of lithium disilicate (Li2Si2O5) glass-ceramic. *J. Mech. Behav. Biomed. Mater.* **2014**, *32*, 345−350.

(7) Du, J.; Corrales, L. R. Structure, dynamics, and electronic properties of lithium disilicate melt and glass. *J. Chem. Phys.* **2006**, *125*, 114702.
(8) Li, C.; Liu, C.; Wang, W.; Mutlu, Z.; Bell, J.; Ahmed, K.; Ye, R.; Ozkan, M.; Ozkan, C. S. Silicon Derived from Glass Bottles as Anode Materials for Lithium Ion Full Cell Batteries. *Sci. Rep.* **2017**, *7*, 917.
(9) Granados, L.; Morena, R.; Takamure, N.; Suga, T.; Huang, S.; McKenzie, D. R.; Ho-Baillie, A. Silicate glass-to-glass hermetic bonding for encapsulation of next-generation optoelectronics: A review. *Mater. Today* **2021**, *47*, 131−155.
(10) Mir, M.; Ali, M. N.; Sami, J.; Ansari, U. Review of Mechanics and Applications of Auxetic Structures. *Adv. Mater. Sci. Eng.* **2014**, *2014*, 1−17.
(11) Morrell, R. *Compr. Compos. Mater.*; Elsevier, 2000; pp 1−24.
(12) Bayya, S. S.; Chin, G. D.; Sanghera, J. S.; Aggarwal, I. D. Germanate glass as a window for high energy laser systems. *Opt. Express* **2006**, *14*, 11687.
(13) Kowada, Y.; Ellis, D. *Adv. Quantum Chem.*; Academic Press, 1998; Vol. *29*; pp 233−251.
(14) Varshneya, A. K.; Mauro, J. C. *Fundam. Inorg. Glas.*; Elsevier, 2019; pp 1−18.
(15) Agrawal, G. *Nonlinear Fiber Opt.*; Elsevier, 2013; pp 457−496.
(16) Peng, L.; Stebbins, J. F. Sodium germanate glasses and crystals: NMR constraints on variation in structure with composition. *J. Non. Cryst. Solids* **2007**, *353*, 4732−4742.
(17) Nanba, T.; Kieffer, J.; Miura, Y. Molecular dynamic simulation on the structure of sodium germanate glasses. *J. Non. Cryst. Solids* **2000**, *277*, 188−206.
(18) Kozhina, E. L.; Shultz, M. M. Thermodynamic properties of sodium-containing glassforming oxide melts. *Ceram. - Silikaty* **2000**, *44*, 91−97.
(19) Doi, A.; Day, D. E. Thermally stimulated polarization current in sodium germanate glass. *J. Mater. Sci.* **1980**, *15*, 3047−3050.
(20) Ginetti, Y. Structure cristalline du métagermanate de sodium. *Bull. des Sociétés Chim. Belges* **1954**, *63*, 460−469.
(21) Füllenkle, H.; Wittmann, A.; Nowotny, H. Verfeinerung der Kristallstruktur des Natriummetagermanats, Na2GeO3. *Monatshefte für Chemie* **1971**, *102*, 964−970.
(22) Cruickshank, D. W. J.; Kálmán, A.; Stephens, J. S. A reinvestigation of sodium metagermanate. *Acta Crystallogr. Sect. B Struct. Crystallogr. Cryst. Chem.* **1978**, *34*, 1333−1334.
(23) McDonald, W. S.; Cruickshank, D. W. J. A reinvestigation of the structure of sodium metasilicate, Na 2 SiO 3. *Acta Crystallogr.* **1967**, *22*, 37−43.
(24) Yan, S.; Wang, J.; Zou, Z. An anion-controlled crystal growth route to Zn2GeO4 nanorods for efficient photocatalytic conversion of CO2 into CH4. *Dalt. Trans.* **2013**, *42*, 12975.
(25) Zachariasen, W. H. THE ATOMIC ARRANGEMENT IN GLASS. *J. Am. Chem. Soc.* **1932**, *54*, 3841−3851.
(26) Du, L.-S.; Stebbins, J. F. Oxygen Sites and Network Coordination in Sodium Germanate Glasses and Crystals: High-Resolution Oxygen-17 and Sodium-23 NMR. *J. Phys. Chem. B* **2006**, *110*, 12427−12437.
(27) KAMIYA, K.; TATSUMI, M.; NASU, H.; MATSUOKA, J. Structure of the Sol-Gel-Derived Sodium Germanate Glass. *J. Ceram. Soc. Japan* **1993**, *101*, 1201−1205.
(28) Huang, W.; Jain, H.; Meitzner, G. The structure of potassium germanate glasses by EXAFS. *J. Non. Cryst. Solids* **1996**, *196*, 155−161.
(29) Di Martino, D.; Santos, L.; Marques, A.; Almeida, R. Vibrational spectra and structure of alkali germanate glasses. *J. Non. Cryst. Solids* **2001**, *293*−*295*, 394−401.
(30) Kresse, G.; Furthmüller, J. Efficient iterative schemes for ab initio total-energy calculations using a plane-wave basis set. *Phys. Rev. B* **1996**, *54*, 11169−11186.
(31) Perdew; Burke; Ernzerhof. Generalized Gradient Approximation Made Simple. *Phys. Rev. Lett.* **1996**, *77*, 3865−3868.
(32) Blöchl, P. E. Projector augmented-wave method. *Phys. Rev. B* **1994**, *50*, 17953−17979.
(33) Monkhorst, H. J.; Pack, J. D. Special points for Brillouin-zone integrations. *Phys. Rev. B* **1976**, *13*, 5188−5192.
(34) Parlinski, K.; Li, Z. Q.; Kawazoe, Y. Ab initio calculations of phonons in $LiNbO_3$. *Phys. Rev. B* **2000**, *61*, 272−278.
(35) Zosiamliana, R.; Lalrinkima; Chettri, B.; Abdurakhmanov, G.; Ghimire, M. P.; Rai, D. P. Electronic, mechanical, optical and piezoelectric properties of glass-like sodium silicate (Na 2 SiO 3) under compressive pressure. *RSC Adv.* **2022**, *12*, 12453−12462.
(36) Khuong Dien, V.; Thi Han, N.; Nguyen, T. D. H.; Huynh, T. M. D.; Pham, H. D.; Lin, M.-F. Geometric and Electronic Properties of Li2GeO3. *Front. Mater.* **2020**, *7*, 288.
(37) West, A. R.; Blake, A. J. Phase equilibria and transformations in the system Li2GeO3-Na2GeO3. *J. Mater. Sci.* **1976**, *11*, 801−808.
(38) Cuautli, C.; Romero-Ibarra, I.; Vazquez-Arenas, J.; Galvan, M. Determination of active sites on Na2SiO3 and Li2SiO3 catalysts for methanol dissociation and methoxide stabilization concerning biodiesel production. *Fuel* **2021**, *298*, 120840.
(39) Mijangos, G. E.; Cuautli, C.; Romero-Ibarra, I. C.; Vazquez-Arenas, J.; Santolalla-Vargas, C. E.; Santes, V.; Castañeda-Galván, A. A.; Pfeiffer, H. Experimental and theoretical analysis revealing the underlying chemistry accounting for the heterogeneous transesterification reaction in Na2SiO3 and Li2SiO3 catalysts. *Renew. Energy* **2022**, *184*, 845−856.
(40) Charpentier, T.; Ispas, S.; Profeta, M.; Mauri, F.; Pickard, C. J. First-Principles Calculation of 17 O, 29 Si, and 23 Na NMR Spectra of Sodium Silicate Crystals and Glasses. *J. Phys. Chem. B* **2004**, *108*, 4147−4161.
(41) Zhang, S.; Wan, S.; Zeng, Y.; Jiang, S.; Gong, X.; You, J. In Situ Raman Spectroscopy and DFT Studies of the Li 2 GeO 3 Melt Structure. *Inorg. Chem.* **2019**, *58*, 5025−5030.
(42) Dien, V. K.; Pham, H. D.; Tran, N. T. T.; Han, N. T.; Huynh, T. M. D.; Nguyen, T. D. H.; Fa-Lin, M. Orbital-hybridization-created optical excitations in Li2GeO3. *Sci. Rep.* **2021**, *11*, 4939.
(43) Bennett, J. W. Exploring the A2BX3Family for New Functional Materials Using Crystallographic Database Mining and First-Principles Calculations. *J. Phys. Chem. C* **2020**, *124*, 19413−19425.
(44) Zosiamliana, R.; Chettri, B.; Fabris, G. S. L.; Sambrano, J. R.; Abdullaev, S.; Abdurakhmanov, G.; Rai, D. P. Electronic, mechanical and piezoelectric properties of glass-like complex Na 2 Si 1 x Ge x O 3 (x = 0.0, 0.25, 0.50, 0.75, 1.0). *RSC Adv.* **2022**, *12*, 27666−27678.
(45) Li, G.; Luican, A.; Lopes dos Santos, J. M. B.; Castro Neto, A. H.; Reina, A.; Kong, J.; Andrei, E. Y. Observation of Van Hove singularities in twisted graphene layers. *Nat. Phys.* **2010**, *6*, 109−113.
(46) Liu, F.; Garofalini, S.; King-Smith, R.; Vanderbilt, D. Structural and electronic properties of sodium metasilicate. *Chem. Phys. Lett.* **1993**, *215*, 401−404.
(47) Baral, K.; Ching, W. Y. Electronic structures and physical properties of Na2O doped silicate glass. *J. Appl. Phys.* **2017**, *121*, 245103.
(48) Subedi, K. N.; Botu, V.; Drabold, D. A. Atomic properties of sodium silicate glasses obtained from the building-block method. *Phys. Rev. B* **2021**, *103*, 134202.
(49) Veena, R.; Srimathi, K.; Puspamitra, P.; Ganapathi Subramaniam, N. Spherical LiZnBO3: Structural, optical and electrochemical properties. *Mater. Sci. Energy Technol.* **2019**, *2*, 267−271.
(50) Rohling, R. Y.; Tranca, I. C.; Hensen, E. J. M.; Pidko, E. A. Correlations between Density-Based Bond Orders and Orbital-Based Bond Energies for Chemical Bonding Analysis. *J. Phys. Chem. C* **2019**, *123*, 2843−2854.
(51) Ching, W. Y.; Murray, R. A.; Lam, D. J.; Veal, B. W. Comparative studies of electronic structures of sodium metasilicate and α and β phases of sodium disilicate. *Phys. Rev. B* **1983**, *28*, 4724−4735.
(52) Mori, Y. *Powder Technol. Handb.*; CRC Press, 2006; pp 143−152.
(53) Cerdeira, F. *Semicond. Semimetals*; Elsevier, 1998; Vol. *56*; pp 225−292.

https://doi.org/10.1021/acsomega.3c00499
ACS Omega 2023, 8, 16869−16882

(54) Tsao, C.-Y.; Weber, J. W.; Campbell, P.; Widenborg, P. I.; Song, D.; Green, M. A. Low-temperature growth of polycrystalline Ge thin film on glass by in situ deposition and ex situ solid-phase crystallization for photovoltaic applications. *Appl. Surf. Sci.* **2009**, *255*, 7028−7035.
(55) Ambrosch-Draxl, C.; Sofo, J. O. Linear optical properties of solids within the full-potential linearized augmented planewave method. *Comput. Phys. Commun.* **2006**, *175*, 1−14.
(56) Xiao, G.; Cao, Y.; Qi, G.; Wang, L.; Liu, C.; Ma, Z.; Yang, X.; Sui, Y.; Zheng, W.; Zou, B. Pressure Effects on Structure and Optical Properties in Cesium Lead Bromide Perovskite Nanocrystals. *J. Am. Chem. Soc.* **2017**, *139*, 10087−10094.
(57) Alam, M. S.; Saiduzzaman, M.; Biswas, A.; Ahmed, T.; Sultana, A.; Hossain, K. M. Tuning band gap and enhancing optical functions of AGeF3 (A = K, Rb) under pressure for improved optoelectronic applications. *Sci. Rep.* **2022**, *12*, 8663.
(58) Joshi, H.; Shankar, A.; Limbu, N.; Ram, M.; Laref, A.; Patra, P. K.; Ismailova, O. B.; Zuala, L.; Chatterjee, S.; Rai, D. P. Pressure-Induced Enhanced Optical Absorption in Sulvanite Compound Cu 3 TaX 4 (X = S, Se, and Te): An ab Initio Study. *ACS Omega* **2022**, *7*, 19070−19079.
(59) Mirdda, J. N.; Mukhopadhyay, S.; Sahu, K. R.; Goswami, M. N. Enhancement of optical properties and dielectric nature of Sm3+doped Na2O−ZnO−TeO2Glass materials. *J. Phys. Chem. Solids* **2022**, *167*, 110776.
(60) Chutithanapanon, N.; Bootjomchai, C.; Laopaiboon, R. Investigation of the optical properties of borosilicate glass recycled from high-pressure sodium lamp glass: Compositional dependence by addition of Bi2O3. *J. Phys. Chem. Solids* **2019**, *132*, 244−251.
(61) Jin, G. L.; Liu, Y.; Mundy, J. N. Refractive index and density of Na-, Rb- and mixed Na, Rb-aluminogermanate glasses. *J. Mater. Sci.* **1987**, *22*, 3672−3678.
(62) Mouhat, F.; Coudert, F.-X. Necessary and sufficient elastic stability conditions in various crystal systems. *Phys. Rev. B* **2014**, *90*, 224104.
(63) Born, M. On the stability of crystal lattices. I. *Math. Proc. Cambridge Philos. Soc.* **1940**, *36*, 160−172.
(64) Xiao, W.; Yang, Y.; Pi, Z.; Zhang, F. Phase Stability and Mechanical Properties of the Monoclinic, Monoclinic-Prime and Tetragonal REMO4 (M = Ta, Nb) from First-Principles Calculations. *Coatings* **2022**, *12*, 73.
(65) Kleinman, L. Deformation Potentials in Silicon. I. Uniaxial Strain. *Phys. Rev.* **1962**, *128*, 2614−2621.
(66) Khandy, S. A.; Islam, I.; Gupta, D. C.; Khenata, R.; Laref, A. Lattice dynamics, mechanical stability and electronic structure of Fe-based Heusler semiconductors. *Sci. Rep.* **2019**, *9*, 1475.
(67) Lalrinkima; Ekuma, C. E.; Chibueze, T. C.; Fomin, L. A.; Malikov, I. V.; Zadeng, L.; Rai, D. P. Electronic, magnetic, vibrational, and X-ray spectroscopy of inverse full-Heusler Fe 2 IrSi alloy. *Phys. Chem. Chem. Phys.* **2021**, *23*, 11876−11885.
(68) Meshalkin, A.; Kaplun, A. Phase equilibria in the Na2O−SiO2 system. *Russian journal of inorganic chemistry* **2003**, *48*, 1567−1569.
(69) Voigt, W. *Lehrbuch der Kristallphysik*; Teubner Verlag Scientific Research Publishing, Leipzig, 1928.
(70) Reuss, A. Berechnung der Fließgrenze von Mischkristallen auf Grund der Plastizitätsbedingung für Einkristalle. *ZAMM - J. Appl. Math. Mech./Zeitschrift für Angew. Math. und Mech.* **1929**, *9*, 49−58.
(71) Hill, R. The Elastic Behaviour of a Crystalline Aggregate. *Proc. Phys. Soc. Sect. A* **1952**, *65*, 349−354.
(72) Zeng, X.; Peng, R.; Yu, Y.; Hu, Z.; Wen, Y.; Song, L. Pressure Effect on Elastic Constants and Related Properties of Ti3Al Intermetallic Compound: A First-Principles Study. *Materials (Basel)* **2018**, *11*, 2015.
(73) Chung, D. H.; Buessem, W. R. The Elastic Anisotropy of Crystals. *J. Appl. Phys.* **1967**, *38*, 2010−2012.
(74) Kube, C. M. Elastic anisotropy of crystals. *AIP Adv.* **2016**, *6*, 095209.
(75) Zhang, H.; Tang, Y.; Zhong, X.; Zhang, Y.; Song, H.; Wang, J.; Wang, Q. The electronic, elastic and thermodynamic properties of carbon-and nitrogen-doped Hf 2 PB: a theoretical approach. *Mater. Res. Express* **2019**, *6*, 056507.
(76) Chen, X.-Q.; Niu, H.; Franchini, C.; Li, D.; Li, Y. Hardness of *T* -carbon: Density functional theory calculations. *Phys. Rev. B* **2011**, *84*, 121405.
(77) Faridi, M.; Tariq, S.; Imran Jamil, M.; Batool, A.; Nadeem, S.; Amin, A. Pressure induced band-gap tuning in KNbO3 for piezoelectric applications: Quantum DFT-GGA approach. *Chin. J. Phys.* **2018**, *56*, 1481−1487.
(78) Chen, H.; Yang, L. Pressure effect on the structural and elastic property of Hf2InC. *Phys. B Condens. Matter* **2011**, *406*, 4489−4493.
(79) Tani, J.-i.; Takahashi, M.; Kido, H. Lattice dynamics and elastic properties of Mg3As2 and Mg3Sb2 compounds from first-principles calculations. *Phys. B Condens. Matter* **2010**, *405*, 4219−4225.
(80) Cahill, D. G.; Pohl, R. Heat flow and lattice vibrations in glasses. *Solid State Commun.* **1989**, *70*, 927−930.
(81) Shan, W.; Walukiewicz, W.; Ager, J. W.; Yu, K. M.; Wu, J.; Haller, E. E. Pressure dependence of the fundamental band-gap energy of CdSe. *Appl. Phys. Lett.* **2004**, *84*, 67−69.
(82) Errandonea, D.; Bandiello, E.; Segura, A.; Hamlin, J.; Maple, M.; Rodriguez-Hernandez, P.; Muñoz, A. Tuning the band gap of PbCrO4 through high-pressure: Evidence of wide-to-narrow semiconductor transitions. *J. Alloys Compd.* **2014**, *587*, 14−20.
(83) Damjanovic, D.; Newnham, R. E. Electrostrictive and piezoelectric materials for actuator applications. *J. Intell. Mater. Syst. Struct.* **1992**, *3*, 190−208.
(84) Aksel, E.; Jones, J. L. Advances in lead-free piezoelectric materials for sensors and actuators. *Sensors* **2010**, *10*, 1935−1954.
(85) Chorsi, M. T.; Curry, E. J.; Chorsi, H. T.; Das, R.; Baroody, J.; Purohit, P. K.; Ilies, H.; Nguyen, T. D. Piezoelectric Biomaterials for Sensors and Actuators. *Adv. Mater.* **2019**, *31*, 1802084.
(86) Zaszczyńska, A.; Gradys, A.; Sajkiewicz, P. Progress in the Applications of Smart Piezoelectric Materials for Medical Devices. *Polymers (Basel)* **2020**, *12*, 2754.
(87) Alsaad, A.; Al-Aqtash, N.; Sabirianov, R. F.; Ahmad, A.; Al-Bataineh, Q. M.; Qattan, I.; Albataineh, Z. First-Principles Calculation of Physical Tensors of α-Diisopropylammonium Bromide (α-DIPAB) Molecular Ferroelectric Crystal. *Front. Phys.* **2019**, *7*, 203.
(88) Tarumi, R.; Nakamura, K.; Ogi, H.; Hirao, M. Complete set of elastic and piezoelectric coefficients of α-quartz at low temperatures. *J. Appl. Phys.* **2007**, *102*, 113508.
(89) Erba, A.; El-Kelany, K. E.; Ferrero, M.; Baraille, I.; Rérat, M. Piezoelectricity of $SrTiO_3$: An *ab initio* description. *Phys. Rev. B* **2013**, *88*, 035102.
(90) Blanco, M.; Francisco, E.; Luaña, V. GIBBS: isothermal-isobaric thermodynamics of solids from energy curves using a quasi-harmonic Debye model. *Comput. Phys. Commun.* **2004**, *158*, 57−72.
(91) Belmonte, D.; Gatti, C.; Ottonello, G.; Richet, P.; Zuccolini, M. V. Ab initio thermodynamic and thermophysical properties of sodium metasilicate, Na2SiO3, and their electron-density and electron-pair-density counterparts. *J. Phys. Chem. A* **2016**, 120.
(92) Holt, A. C.; Ross, M. Calculations of the Grüneisen Parameter for Some Models of the Solid. *Phys. Rev. B* **1970**, *1*, 2700−2705.
(93) White, G.; Birch, J.; Manghnani, M. H. Thermal properties of sodium silicate glasses at low temperatures. *J. Non. Cryst. Solids* **1977**, *23*, 99−110.

https://doi.org/10.1021/acsomega.3c00499
ACS Omega 2023, 8, 16869−16882